Effects of initial-state dynamics on collective flow within a coupled transport and viscous hydrodynamic approach

Chandrodoy Chattopadhyay, Rajeev S. Bhalerao, Jean-Yves Ollitrault,
Subrata Pal

Effects of initial-state dynamics on collective flow within a coupled transport and viscous hydrodynamic approach

Chandrodoy Chattopadhyay,[1] Rajeev S. Bhalerao,[2] Jean-Yves Ollitrault,[3] and Subrata Pal[1]

[1]*Department of Nuclear and Atomic Physics, Tata Institute of Fundamental Research, Homi Bhabha Road, Mumbai 400005, India*
[2]*Department of Physics, Indian Institute of Science Education and Research (IISER), Homi Bhabha Road, Pune 411008, India*
[3]*CNRS, URA2306, IPhT, Institut de physique théorique de Saclay, F-91191 Gif-sur-Yvette, France*

We evaluate the effects of preequilibrium dynamics on observables in ultrarelativistic heavy-ion collisions. We simulate the initial nonequilibrium phase within a multiphase transport (AMPT) model, while the subsequent near-equilibrium evolution is modeled using (2+1)-dimensional relativistic viscous hydrodynamics. We match the two stages of evolution carefully by calculating the full energy-momentum tensor from AMPT and using it as input for the hydrodynamic evolution. We find that when the preequilibrium evolution is taken into account, final-state observables are insensitive to the switching time from AMPT to hydrodynamics. Unlike some earlier treatments of preequilibrium dynamics, we do not find the initial shear viscous tensor to be large. With a shear viscosity to entropy density ratio of 0.12, our model describes quantitatively a large set of experimental data on Pb+Pb collisions at the Large Hadron Collider over a wide range of centrality: differential anisotropic flow $v_n(p_T)(n = 2\text{–}6)$, event-plane correlations, correlation between v_2 and v_3, and cumulant ratio $v_2\{4\}/v_2\{2\}$.

I. INTRODUCTION

High-energy heavy-ion collision experiments at the Relativistic Heavy-Ion Collider (RHIC) [1,2] and at the Large Hadron Collider (LHC) [3–5] have established the formation of a strongly interacting quark-gluon plasma (QGP). Evidence is based on the large collective flow observed in the plane transverse to the beam axis, in particular the anisotropic flow. These observations can be explained by treating the formed QGP as a viscous relativistic fluid [6–9], with a small shear viscosity to entropy density ratio η/s [10], corresponding to a strongly interacting system [11]. The flow is found to originate mostly from the early, partonic stage of the expansion. It is therefore essential to scrutinize its sensitivity to the early dynamics, in particular, to the early stages where hydrodynamics cannot be applied.

The initial stage, defined as the stage after which the hydrodynamic description is permissible, is the largest source of uncertainty in hydrodynamic modeling. Not only is the initial energy density profile poorly constrained [12,13], the matter formed is also out of equilibrium in several respects. First, the expansion into the vacuum generates significant transverse flow at early times, which must be taken into account when setting up realistic initial conditions for hydrodynamics [14,15]. Second, due to the rapid longitudinal expansion, the pressure is strongly anisotropic at early times [16] (the longitudinal pressure is smaller than the transverse pressure), which has triggered the development of anisotropic hydrodynamics [17,18]. Both effects, initial flow and pressure anisotropy, are encoded in the energy-momentum tensor $T^{\mu\nu}$ used as an initial condition for hydrodynamic calculations. Therefore, a proper approach to preequilibrium dynamics is to model the full $T^{\mu\nu}$. This has first been done in the context of strong-coupling

calculations [19], and more recently in the weak-coupling regime [20,21]. However, there are to date few hydrodynamic calculations using as input the full energy-momentum tensor $T^{\mu\nu}$ resulting from a consistent model of the early dynamics [19,22]. For instance, the IP-Glasma+MUSIC calculation of Ref. [23] does not conserve the full $T^{\mu\nu}$ when switching from classical gluon dynamics to hydrodynamics and neither does the recent superSONIC calculation of Ref. [24].

In this paper, we use the multiphase transport model AMPT [25] to model the preequilibrium dynamics. AMPT implements realistic cross sections between particles. It thus complements previous idealized approaches using weak-coupling or strong-coupling techniques. AMPT is able to simulate the entire collision event, but we use it here only to model the initial stages. It has been used earlier as an input to ideal [26] and viscous [27,28] hydrodynamic calculations, but at the expense of discarding part of the information contained in $T^{\mu\nu}$. Here, we switch from AMPT to (2+1)-dimensional second-order viscous hydrodynamics [29] by matching the full $T^{\mu\nu}$. The details of this hybrid model are described in Sec. II. In Sec. III, we discuss the sensitivity of hydrodynamic flow to the initial stages. In Sec. IV, we compare the results of our model with several LHC data on Pb+Pb collisions at 2.76 and 5.02 TeV: transverse-momentum spectra, anisotropic flow, correlations between flow magnitudes in different harmonics, two- and three-event-plane correlators.

II. MODEL AND INITIAL CONDITIONS

The AMPT model [25] is a widely used transport model, which provides a good description of several observables of heavy-ion collisions, in particular pair correlations [30] and anisotropic flow [31,32], over a wide range of colliding

energies [33]. AMPT has also been able to predict quantitatively the magnitudes of event-plane correlations [34,35] and other multiparticle correlations [36]. The AMPT version implemented in this paper uses the HIJING 2.0 model [37,38] to determine the nucleon configuration in an event. Nucleons can undergo soft collisions, which lead to string excitations, and hard collisions, which produce minijet partons [39]. We have employed the string melting version of AMPT [25], in which strings are melted into their constituent quarks and antiquarks, and which improves the description of the anisotropic flow data. The scatterings among these quarks and minijet partons and their evolution are treated with ZPC parton cascade [40] with a parton-parton elastic cross section of 1.5 mb.

While AMPT by itself can simulate the entire collision event, we use it here only to describe the first stages, and then couple it to a viscous hydrodynamic description. The hydrodynamic code we use [29] is (2+1) dimensional, in the sense that it assumes boost invariance in the longitudinal direction [41] and determines numerically the transverse flow only. This choice is motivated by simplicity, and by the observation that anisotropic flow depends little on rapidity [4,42,43]. We thereby neglect the effect of longitudinal fluctuations [44–52], which have been much studied lately, but mildly affect flow observables near midrapidity. The transition from AMPT to hydrodynamics is implemented on a constant proper time hypersurface $\sqrt{t^2 - z^2} = \tau_{\rm sw}$. Since the AMPT model is (3+1) dimensional, we need to project it as we switch to the (2+1)-dimensional hydrodynamic model. This is achieved by averaging over the space-time rapidity η_s, defined as $\eta_s \equiv (1/2)\ln[(t+z)/(t-z)]$, in the window $-3 < \eta_s < 3$.[1] We include all particles in this window and consider only their longitudinal momenta relative to the fluid. In the Bjorken picture [41], the longitudinal fluid velocity is $v_z = z/t$. Therefore, the longitudinal motion relative to the fluid is obtained by transforming the energy and longitudinal momentum as follows:

$$E' = E\cosh\eta_s - p_z\sinh\eta_s,$$
$$p'_z = p_z\cosh\eta_s - E\sinh\eta_s. \qquad (1)$$

The transverse momentum is unchanged: $p'_T = p_T$.

We now describe how the energy-momentum $T^{\mu\nu}$ is evaluated. Switching from a discrete description, in terms of pointlike particles, to a continuous description, in terms of a fluid, typically involves a coarse-graining procedure, where one defines a fluid element by the particles it contains. We choose an alternative procedure and treat each particle as an extended object, whose size is much larger than the transverse distance between particles, so that the fluid formed by all the particles is smooth. Specifically, we smear each parton in AMPT by two-dimensional (2D) Gaussian distribution in the transverse plane [53]. $T^{\mu\nu}$ is defined at each point as

$$T^{\mu\nu}(x, y) = \frac{1}{2\pi\sigma^2\tau_{\rm sw}\Delta\eta_s} \sum_i \frac{p_i'^{\mu}p_i'^{\nu}}{p_i'^0}$$
$$\times \exp\left[-\frac{(x - x_i)^2 + (y - y_i)^2}{2\sigma^2}\right], \qquad (2)$$

where the sum runs over all partons i with transverse coordinates (x_i, y_i) and energies $E'_i \equiv p_i'^0 = \sqrt{\mathbf{p}_i'^2 + m_i^2}$, and $\Delta\eta_s = 6$ is the width of the η_s window. The Gaussian transverse width is a free parameter, which we set to $\sigma = 0.8$ fm.

The energy-momentum tensor in viscous hydrodynamics is usually written as [54]

$$T^{\mu\nu} = \epsilon u^{\mu}u^{\nu} - (P + \Pi)\Delta^{\mu\nu} + \pi^{\mu\nu}, \qquad (3)$$

where u^{μ} is the fluid four-velocity, ϵ and P are the energy density and pressure in the fluid's local rest frame, $\Delta^{\mu\nu} = g^{\mu\nu} - u^{\mu}u^{\nu}$ is the projection operator on the three-space orthogonal to u^{μ} defined in the Landau frame, Π is the bulk pressure, and $\pi^{\mu\nu}$ is the shear pressure tensor. We now explain how the quantities in the right-hand side of Eq. (3) are obtained from $T^{\mu\nu}$. ϵ and u^{μ} are given by the Landau matching condition:

$$T^{\mu\nu}u_{\nu} = \epsilon u^{\mu}. \qquad (4)$$

The pressure P is then related to ϵ by the equation of state. We have employed the s95p-PCE equation of state [55], which is obtained from fits to lattice data for crossover transition and matches a realistic hadron resonance gas model at low temperatures T, with partial chemical equilibrium (PCE) of the hadrons at temperatures below $T_{\rm PCE} \approx 165$ MeV.

The bulk pressure Π is then obtained from the trace:

$$T^{\mu}_{\mu} = \epsilon - 3(P + \Pi). \qquad (5)$$

Using Eq. (2), the contribution of each parton to T^{μ}_{μ} is proportional to $p^{\mu}p_{\mu} = m^2$. The masses of partons in AMPT are current quark masses, which are small for light quarks, so that the bulk pressure Π is small. We neglect it in the present calculation. Finally, the shear pressure tensor $\pi^{\mu\nu}$ is given by Eq. (3).

Our procedure conserves the full structure of the energy momentum tensor from the initial stage, and therefore automatically includes the effect of initial transverse flow and a viscous corrections to the pressure tensor. The resulting initial conditions are more realistic than typical prescriptions where $\pi^{\mu\nu}$ is set to 0 [24] or initialized to the Navier-Stokes value [56]. Our transport calculation also takes into account interactions before the start of hydrodynamics. The resulting hybrid calculation is more consistent in this respect than that of Ref. [15], where the preequilibrium stage is modeled by free-streaming partons. Naturally, at the instant of switchover to hydrodynamics, the system in Ref. [15] is far from equilibrium with a large shear viscous tensor, whereas in the present work the preequilibrium dynamics drives the system close to local equilibrium, allowing a smooth matching to the hydrodynamics at the switch-over time. We account for the full preequilibrium dynamics, as was done previously in Refs. [19,22].

The hydrodynamic evolution is continued till each fluid cell reaches a decoupling temperature of $T_{\rm dec} = 120$ MeV. The hadronic spectra are obtained at this temperature using the Cooper-Frye prescription [57]:

$$\frac{dN}{d^2p_T dy} = \frac{g}{(2\pi)^3} \int p_{\mu}d\Sigma^{\mu} f(x, p), \qquad (6)$$

---

[1] We choose a large rapidity window to maximize the statistics.

where g is the degeneracy, p^μ is the four-momentum of the particle, $d\Sigma^\mu$ represents the element of the 3D freeze-out hypersurface and $f(x, p) = f_0 + \delta f$ is the nonequilibrium phase-space distribution function at freeze out. We have used the standard viscous correction form corresponding to Grad's 14-moment approximation [58]:

$$\delta f = \frac{f_0 \tilde{f}_0}{2(\epsilon + P)T^2} \, p^\alpha p^\beta \pi_{\alpha\beta}, \tag{7}$$

where corrections up to second order in momenta are present, and $\tilde{f}_0 \equiv 1 - r f_0$, with $r = 1, -1, 0$, are the equilibrium distributions for the Fermi, Bose, and Boltzmann gases, respectively. Resonances of masses up to about 2.25 GeV are included in the calculations to be consistent with the s95p-PCE equation of state, and the results presented include the resonance decays.

In this work, we neglect the temperature dependence of the shear viscosity over entropy ratio η/s [59]. We choose the value $\eta/s = 0.12$, which gives a good description of anisotropic flow data (see Sec. IV).

The initial conditions from AMPT need to be adjusted. The reason is that the multiplicity obtained in the AMPT+hydrodynamics model is slightly smaller than that obtained using the AMPT model alone, which matches experimental data. This can be due to the projection from three to two dimensions when we switch from AMPT to hydrodynamics, or from a difference between the effective viscosity in the AMPT calculation and that used in the hydrodynamic calculation. We therefore rescale the initial energy density profile of the hydrodynamic calculation [15] by a constant factor. The value of this factor, which is roughly 1.2, is determined by fitting the charged multiplicity density dN_{ch}/dy to 2.76 TeV LHC data in the 0–5 % centrality range. We use the same factor for other centralities and other colliding energies.

III. EFFECTS OF PREEQUILIBRIUM DYNAMICS

We study the sensitivity of collective flow to the preequilibrium dynamics. For this purpose, we generate 300 Pb+Pb collisions at $\sqrt{s_{NN}} = 5.02$ TeV in the 40–50 % centrality interval, where elliptic flow in the reaction plane is largest [60]. Throughout this article, the centrality c is defined according to impact parameter b by $c = \pi b^2 / \sigma$ [61], with a nucleus-nucleus total inelastic cross section of $\sigma = 784$ and 796 fm² for collisions at $\sqrt{s_{NN}} = 2.76$ and 5.02 TeV, respectively, as calculated from the Glauber model [27].

We first test the sensitivity to the preequilibrium dynamics by varying the initialization of the hydrodynamic calculation. Specifically, we compare the default version, where the full $T^{\mu\nu}$ is evaluated using AMPT (shown as red solid lines in Figs. 1 and 2), with three simplified versions: a fully simplified version where both the initial shear tensor $\pi^{\mu\nu}$ and the transverse velocity v_T are set to 0 (black dotted lines), corresponding to traditional hydrodynamic calculations [56] where the initial conditions are specified solely by the initial energy density profile; one where the transverse velocity is set to zero and the shear tensor to the Navier-Stokes value $\pi^{\mu\nu} = 2\eta\sigma^{\mu\nu}$ [9,56] (green dotted lines); and one where one keeps the transverse velocity but sets the shear tensor $\pi^{\mu\nu}$ to
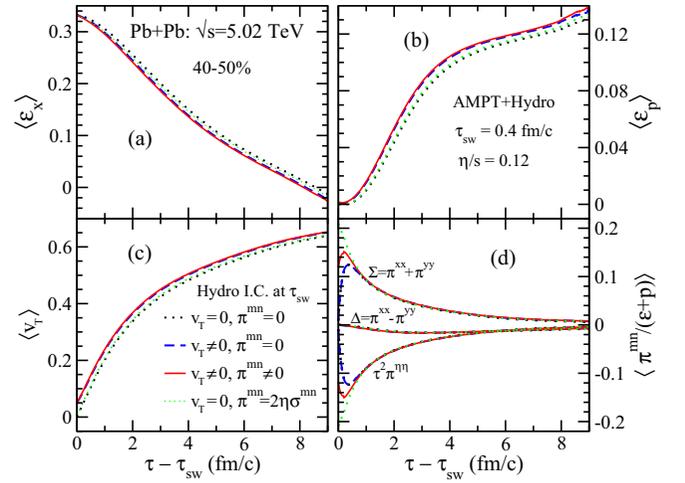

FIG. 1. Time evolution of (a) the eccentricity in the reaction plane, (b) the momentum anisotropy, (c) the transverse flow velocity, and (d) various components of the shear pressure tensor π^{mn} normalized by the enthalpy density. Averages over the transverse plane in (a), (c), and (d) are evaluated with a Lorentz contracted energy density as weight [15]. All quantities are averaged over events. Each panel compares four different initializations (see text). The switching time between AMPT and hydrodynamics is $\tau_{sw} = 0.4$ fm/c.

0 (blue dashed lines). In this way, we can test separately the effects of initial flow and initial shear tensor.

Figure 1 displays the time evolution of various quantities in the hydrodynamic phase. The spatial eccentricity in the reaction plane ε_x [62,63] is shown in Fig. 1(a). Its initial value is large, corresponding to the almond-shaped area of the
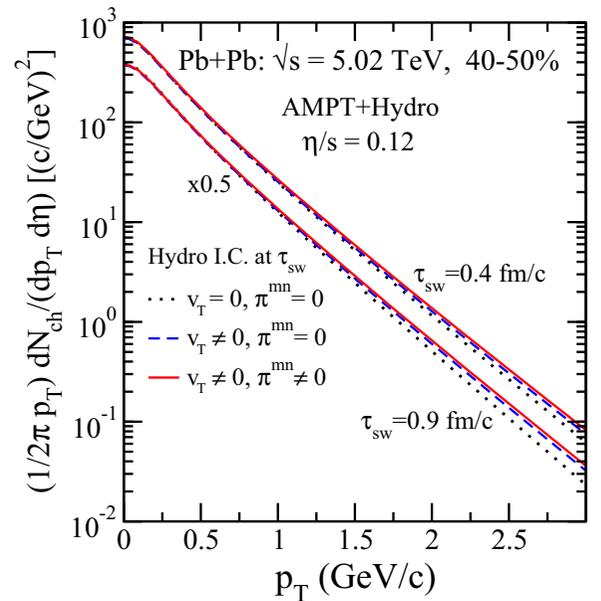

FIG. 2. Transverse momentum spectra of charged particles from the AMPT+hydro calculations. The results are for two switching times $\tau_{sw} = 0.4$ and 0.9 fm/c and three different initial conditions. Curves for $\tau_{sw} = 0.9$ fm/c are shifted vertically in order to avoid overlapping.

overlap region between the nuclei (the impact parameter is in the range 10–11 fm). As the system expands in all directions, its shape becomes rounder and the spatial eccentricity decreases [64]. This decrease is slightly faster if initial transverse flow is included.

The spatial eccentricity creates a momentum anisotropy due to pressure gradients [65], corresponding to elliptic flow. The momentum anisotropy is defined as [56]

$$\varepsilon_p \equiv \frac{\int d^2 r_\perp (T^{xx} - T^{yy})}{\int d^2 r_\perp (T^{xx} + T^{yy})}. \tag{8}$$

Figure 1(b) shows that ε_p develops in the first few fm/c of the expansion [66], as the spatial anisotropy ε_x decreases. The sensitivity of ε_p to preequilibrium dynamics is small, but clearly visible.[2] When initial transverse flow is present, the momentum anisotropy is larger and develops earlier. Note, however, that the value of ε_p at $\tau = \tau_{sw}$ is close to 0, even if initial flow is included. The effect of the initial shear pressure is much smaller than that of initial flow. It only increases slightly the anisotropy, due to the larger transverse pressure. The mean transverse flow velocity, displayed in Fig. 1(c), follows the same pattern, showing that radial flow and elliptic flow are closely related. The inclusion of initial flow imparts a small transverse kick (about 5% of the speed of light) at τ_{sw}.

Figure 1(d) shows the time evolution of the dominant components of the viscous pressure tensor, namely, $\tau^2 \pi^{\eta\eta}$, the sum $\Sigma = \pi^{xx} + \pi^{yy}$ and the difference $\Delta = \pi^{xx} - \pi^{yy}$, all normalized by the enthalpy density. The initial values arising from the AMPT preequilibrium dynamics are about 12% for the first two of these three components. This is in contrast with Ref. [23] where $\pi^{\mu\nu}$ arising from the preequilibrium dynamics was too large and had to be arbitrarily set to zero.[3] Note also that AMPT initial values for $\tau_{sw}^2 \pi^{\eta\eta}$ and Σ are about 40% smaller than Navier-Stokes values. As time evolves, the magnitudes of all three components at first increase due to additional contributions from the viscous hydrodynamics VISH2+1. Thereafter, they all decrease and become negligible at late times [9]. The sensitivity to the initial value of $\pi^{\mu\nu}(\tau_{sw})$ (0, Navier-Stokes, or AMPT) is only visible in the first 1 fm/c: The curves then all converge to the same value. This explains why the results shown in Figs. 1(b) and 1(c) have little sensitivity to the initial value of the shear tensor.

Figure 2 shows the transverse momentum spectra of charged hadrons with different initialization schemes. Transverse flow tends to increase the transverse momentum. We have seen in Fig. 1(c) that initial flow increases the transverse flow at later times. Therefore, it results in more particles at larger p_T. Inclusion of the initial shear tensor has a smaller effect, and goes in the same direction. We also display results with a larger

value of the switching time $\tau_{sw} = 0.9$ fm/c. This leads to a larger initial flow from preequilibrium dynamics in AMPT but leaves less time to develop hydrodynamic flow in VISH2+1. The net effect is a slightly softer spectrum compared to that for 0.4 fm/c.

Figure 3 displays the anisotropic flow coefficients $v_2(p_T)$ to $v_5(p_T)$. They are computed for each hydro event using the usual formulas [67]. The average over events is evaluated in a way that closely follows the experimental procedure: $v_n(p_T)$ is measured by correlating a particle in a given p_T window with a second particle belonging to the same event, but without any restriction on p_T, and then averaging over events. The corresponding formulas in hydrodynamics are written explicitly in Ref. [67]. Specifically, the quantity we evaluate is the "two-particle cumulant flow" as defined in this reference.

Figure 3(a) compares the values of v_n obtained for two different switching times $\tau_{sw} = 0.4$ fm/c (black dotted lines) and 0.9 fm/c (green dashed lines). In this calculation both the transverse velocity and viscous tensor are set to zero at the switching times. Hence, any preequilibrium buildup of flow is ignored here. A delayed start of hydrodynamics at $\tau_{sw} = 0.9$ fm/c leaves less time for the hydrodynamic buildup of momentum anisotropy. This causes a slight reduction in $v_n(p_T)$ as compared to the earlier switching time 0.4 fm/c. The effect is more pronounced for higher flow harmonics. Figure 3(b) is similar to Fig. 3(a) except that the full preequilibrium dynamics from AMPT is included. This results in a slight increase of v_n, as expected from Fig. 1(b). Remarkably, the sensitivity to the switching time becomes negligible once preequilibrium dynamics is included. This means that it is essentially equivalent to run AMPT or viscous hydrodynamics at early times [14].

In Fig. 3(c) we compare $v_n(p_T)$ for various initial conditions at a fixed $\tau_{sw} = 0.4$ fm/c. Compared to the initial $v_T = 0$ case, the inclusion of transverse flow at the switching time injects an additional (finite but small) flow anisotropy at the start of VISH2+1 [see Fig. 1(b)]. This results in a slight enhancement of $v_n(p_T)$ for nonzero flow initialization (blue dashed lines) as compared to the flow-free case (black dotted lines). Further inclusion of viscous tensor has insignificant effect on $v_n(p_T)$ (red solid lines) as hydrodynamic evolution ceases to remember the initial $\pi^{\mu\nu}$ values [see Fig. 1(d)].

In summary, preequilibrium dynamics increases the transverse flow, but this is a small increase as long as the switching time is small. The calculations presented in the next section are carried out with the full preequilibrium dynamics from AMPT.

IV. COMPARISON WITH LHC DATA

We now compare the results of the AMPT+hydro hybrid model calculations with various experimental data for Pb+Pb collisions at the LHC, at energies $\sqrt{s_{NN}} = 2.76$ and 5.02 TeV. Results shown in this section are obtained by generating 300 AMPT+Hydro events per centrality bin up to 40% centrality, and 500 events per bin above 40%.

Figure 4 shows the transverse momentum spectra of pions, kaons and protons in the 0–5 % and 30–40 % central Pb+Pb collisions at $\sqrt{s_{NN}} = 2.76$ TeV in comparison with the ALICE data at midrapidity [68]. The hybrid model shows a good
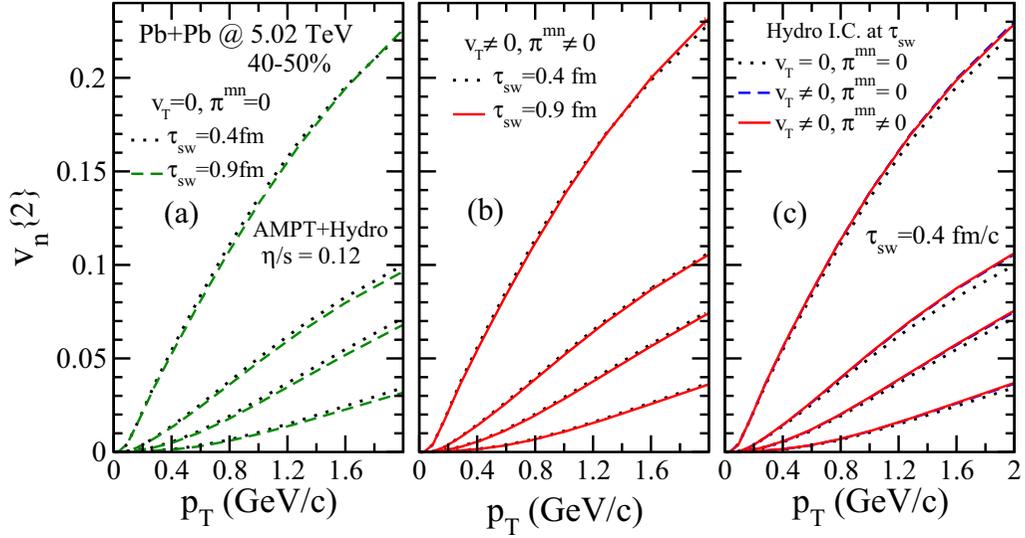
---

[2]We switch to hydrodynamics at an early time $\tau_{sw} = 0.4$ fm/c, therefore the preequilibrium phase does not last long and its effect is limited.

[3]This reference, however, does not give quantitative information about the viscous tensor. Since we have a more realistic microscopic dynamics in the early stage including realistic parton-parton elastic cross sections, it is plausible that our early dynamics drives the system toward local equilibrium more efficiently.

FIG. 3. Anisotropic flow coefficients, $v_n\{2\}(p_T)$ (for $n = 2$–5, top to bottom), for charged hadrons in the AMPT+hydro calculations. (a) Initial flow and viscous tensor set to 0, and two different switching times, $\tau_{sw} = 0.4$ fm/c (black dotted lines) and 0.9 fm/c (green dashed lines). (b) With initial flow and viscous tensor from AMPT. (c) Results for three initial conditions at $\tau_{sw} = 0.4$ fm/c.

agreement with the π^+ and K^+ spectra up to $p_T \sim 2$ GeV. The protons being heavier undergo a strong blue shift due to the radial flow. Our results for protons agree quite well with the data at high p_T. The overprediction in the proton yields at low p_T, may be due to the neglect of massive hadrons ($m \geqslant 2.2$ GeV) and final-state hadron rescattering. Also shown are the predictions of identified hadron spectra for Pb+Pb collisions at $\sqrt{s_{NN}} = 5.02$ TeV (dashed lines). The larger initial temperature at this higher collision energy leads to somewhat harder particle spectra [69]. Note that AMPT alone

(with string melting) yields p_T spectra, which are too soft [25], so that coupling to hydrodynamics improves agreement with data.

Figure 5 compares the anisotropic flow of charged hadrons (v_2 to v_6) from our simulation with the event-plane results from the ATLAS Collaboration [4] at $\sqrt{s_{NN}} = 2.76$ TeV Pb+Pb collisions for various centralities. As explained in Sec. III, our results are obtained by a two-particle correlation method, which differs only slightly [70] from the event-plane method used by ATLAS, for realistic values of the event-plane resolution. Our hybrid calculations are in good agreement with
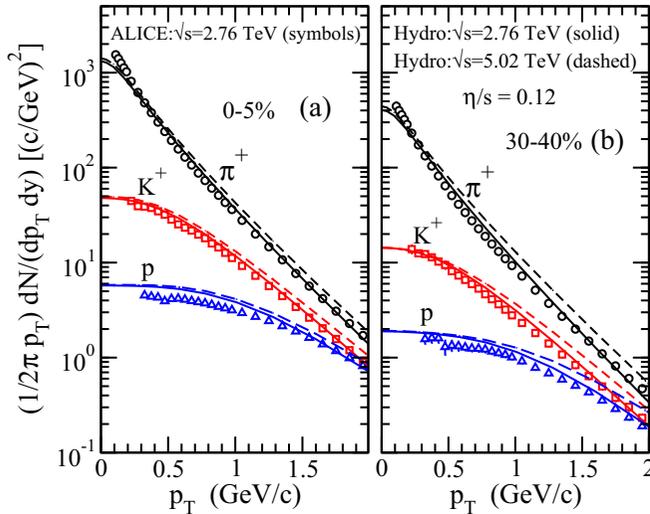

FIG. 4. Transverse momentum spectra of pions, kaons, and protons at midrapidity for two centrality ranges, 0–5 % and 30–40 % in Pb+Pb collisions at $\sqrt{s_{NN}} = 2.76$ TeV in the AMPT+hydro model (solid lines) as compared to the ALICE data [68] (symbols). Model predictions of the particle spectra for Pb+Pb collisions at $\sqrt{s_{NN}} = 5.02$ TeV are shown as dashed lines.
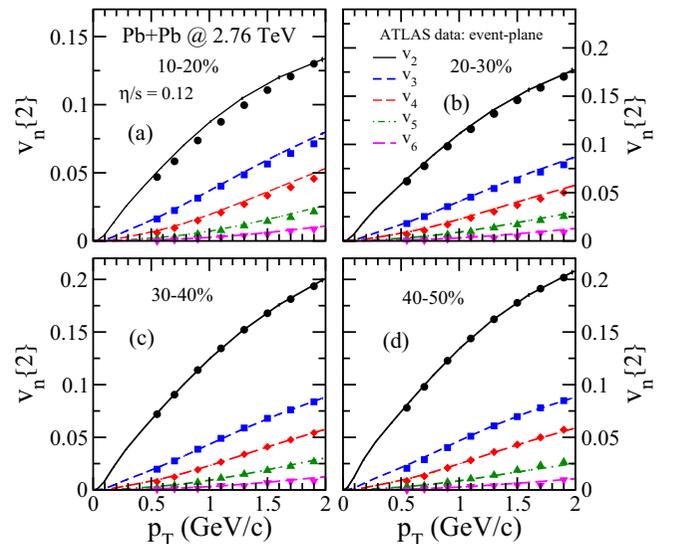

FIG. 5. Anisotropic flow of charged hadrons (top to bottom: v_2 to v_6) as a function of transverse momentum in Pb+Pb collisions at $\sqrt{s_{NN}} = 2.76$ TeV in four centrality windows. Lines: AMPT+Hydro calculations; Symbols: ATLAS data [4].
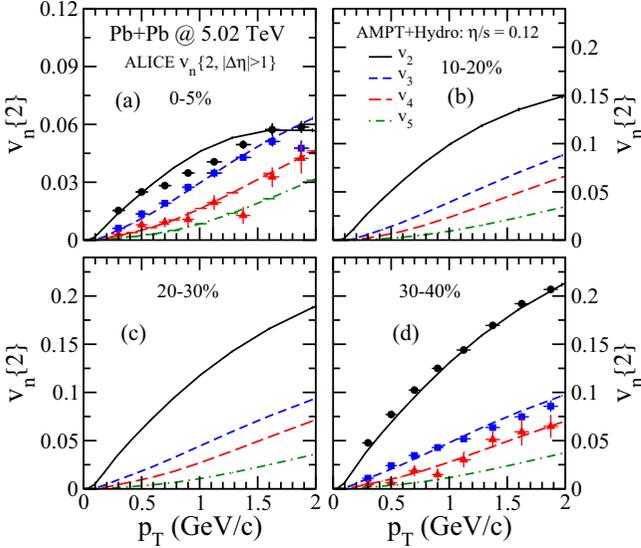
FIG. 6. Anisotropic flow in Pb+Pb collisions at $\sqrt{s_{NN}} = 5.02$ TeV in 4 centrality windows. Lines: AMPT+Hydro calculations; Symbols: ALICE data for v_2, v_3, and v_4 [74].

data over the entire p_T range studied, for all the flow harmonics $n = 2$–6, and over a broad centrality range.

Note that by coupling AMPT to hydrodynamics, we have introduced two free parameters, the width σ in Eq. (2) and the viscosity over entropy ratio η/s (recall that results are essentially independent of the switching time τ_{sw} if one keeps the full $T^{\mu\nu}$ when switching from AMPT to hydrodynamics, as shown in Sec. III). Larger η/s reduces v_n [8], and smaller σ increases the granularity and increases v_3. The chosen values $\sigma = 0.8$ fm and $\eta/s = 0.12$ optimize the description of LHC data.

In particular, agreement is better for this AMPT+hydro model than with AMPT alone, which underpredicts v_n already at $p_T = 2$ GeV [71,72]. Note that most initial-state models with subsequent hydrodynamic evolution are found incompatible with all the flow harmonics even at a given collision centrality [73].

The study is extended to the higher energy $\sqrt{s_{NN}} = 5.02$ TeV in Fig. 6. Figures 6(a) and 6(d) display ALICE data [74]. The higher collision energy ensures a slightly larger $v_n(p_T)$ as the VISH2+1 starts with a somewhat higher initial flow anisotropy. Further, the stronger radial flow blue shifts the anisotropies to higher p_T, especially for the heavier charged hadrons [69,75]. The model provides a good description of the $v_n(p_T)$, ($n = 2$ to 4) data at 30–40 % centrality, and $v_n(p_T)$, ($n = 3$–4) data at 0–5% centrality. It, however, over-predicts somewhat the v_2 data at intermediate p_T for the 0–5 % centrality collisions. Figures 6(b) and 6(c) present our predictions at two other centralities.

Correlations between event planes Ψ_n of different harmonics represent higher-order correlations, which can provide crucial information on the initial state of the matter [3,76] and on the hydrodynamic response [77]. The ATLAS [76] and ALICE [78] Collaborations have measured several such correlations between different harmonics Ψ_n and Ψ_m (with

$n \neq m$). There are two-plane correlations, such as:

$$\langle \cos 4(\Psi_2 - \Psi_4)\rangle_w \equiv \frac{\langle V_2^2 V_4^* \rangle}{\sqrt{\langle V_2^2 V_2^{*2}\rangle}\sqrt{\langle V_4 V_4^*\rangle}}, \qquad (9)$$

where the left-hand side is the quantity measured by ATLAS using the scalar-product method [34,79], and the right-hand side its expression in a hydrodynamic calculation [77], where V_n is the complex anisotropic flow, and angular brackets represent an average over events in a centrality class. Similarly, the three-plane correlator between harmonics 2, 3, and 5 is defined by ATLAS as[4]

$$\langle \cos 2\Psi_2 + 3\Psi_3 - 5\Psi_5 \rangle_w \equiv \frac{\langle V_2 V_3 V_5^* \rangle}{\sqrt{\langle V_2 V_2^*\rangle\langle V_3 V_3^*\rangle\langle V_5 V_5^*\rangle}}. \qquad (10)$$

The two-plane and three-plane correlators evaluated in this paper are listed in Table I of Ref. [34]. In our calculation of event-plane correlations, we use the same cuts as ATLAS [76], viz., $\eta_c \equiv |\eta| = 0$–2.5 and $p_{T_{min}} = 0.5$ GeV.

Figure 7 displays the centrality dependence of two-plane correlations in our AMPT+Hydro calculations. Theoretical results are in good agreement with ATLAS data. Most correlations are large, and driven by the nonlinear hydrodynamic response that couples v_4 to $(v_2)^2$ and v_6 to $(v_2)^3$ [81]. Their increase from central to peripheral collisions is dominated by the increase of v_2. The only exception is the correlation between Ψ_2 and Ψ_3 [Fig. 7(d)], which is much smaller and whose interpretation in terms of hydrodynamic response is less simple [77]. This correlation is also very well described by our event-by-event calculation.

Also shown here are the initial-state correlations calculated with the participant-plane angles Φ_n [63]:

$$\varepsilon_n e^{in\Phi_n} \equiv -\frac{\int d^2 r_\perp \, \gamma(\mathbf{r}_\perp) \, e(\mathbf{r}_\perp) \, r_\perp^n \, e^{in\phi}}{\int d^2 r_\perp \, \gamma(\mathbf{r}_\perp) \, e(\mathbf{r}_\perp) \, r_\perp^n}, \qquad (11)$$

where $e(\mathbf{r}_\perp)$ is the initial energy density, $\gamma(\mathbf{r}_\perp)$ is the Lorentz contraction factor due to the transverse flow [15], the integral runs over the transverse plane in a centered coordinate system [63]. These correlations characterize the initial stage of the hydrodynamic calculations. Our results are qualitatively consistent with those presented in Ref. [82].

The centrality dependence of the three-plane correlations is shown in Fig. 8. Here again, the final-state correlations are in good agreement with the ATLAS data [76]. The correlation between Ψ_2, Ψ_3, and Ψ_5 [Fig. 8(a)] is large and driven by the nonlinear response. That between Ψ_2, Ψ_3, and Ψ_4 [Fig. 8(b)], on the other hand, is smaller in magnitude and lacks a simple explanation in terms of nonlinear response [77], but is well reproduced in event-by-event hydrodynamics [82].

Figure 9 displays the centrality dependence of v_2 and v_3 in the (v_2, v_3) plane, measured by ATLAS [83] in Pb+Pb

___

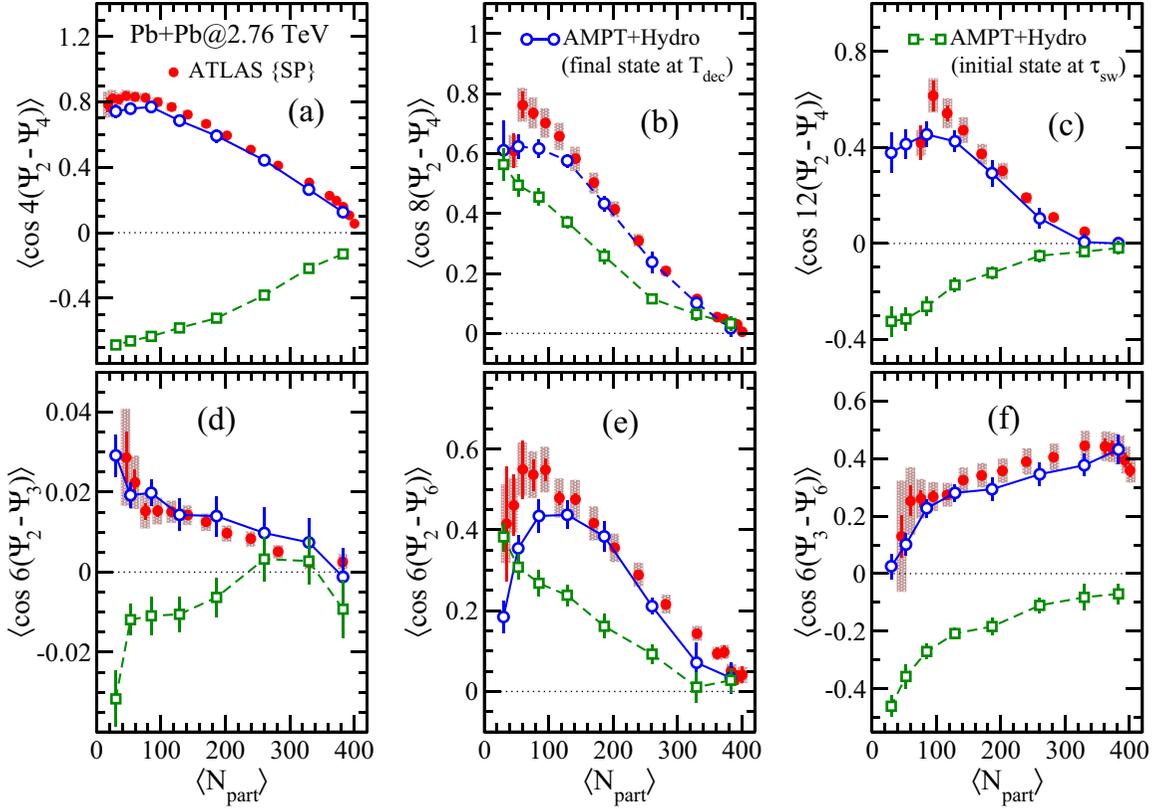[4]ALICE uses a slightly different normalization [78,80].

FIG. 7. Two-plane correlations obtained in the initial-state (open squares) and final-state (open circles) as a function of the number of participants in Pb+Pb collisions at $\sqrt{s_{NN}} = 2.76$ TeV in the AMPT+Hydro model as compared to the ATLAS data [76] using the scalar-product method (solid circles).

collisions at $\sqrt{s_{NN}} = 2.76$ TeV, together with our calculation in AMPT+Hydro. A boomeranglike shape is observed. The corresponding plot for the initial eccentricities ε_2 and ε_3, calculated from Eq. (11) at the switching time $\tau_{sw} = 0.4$ fm/c, is also shown in the inset of Fig. 9. In most central collisions $\varepsilon_2 \approx \varepsilon_3$, and ε_2 increases faster than ε_3 up to about 45% centrality. For more peripheral collisions, the large fluctuations in the small initial geometry contribute to faster rise in ε_3 than ε_2. In fact, the turning around seen in the v_2-v_3 plane, occurs
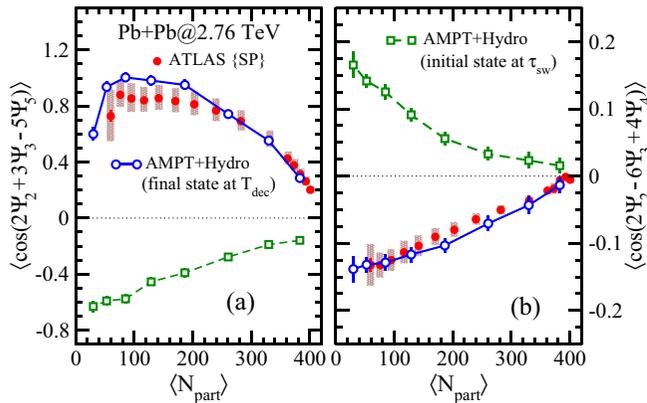

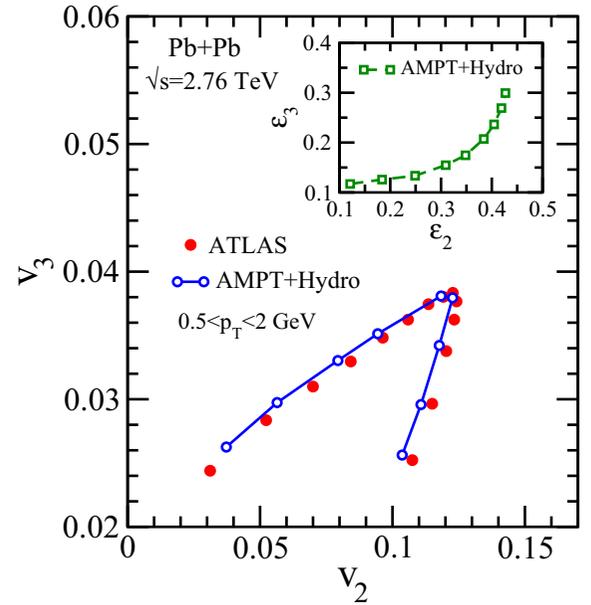FIG. 8. Same as Fig. 7, but for three-plane correlations.

FIG. 9. The correlation between v_2 and v_3 for $0.5 < p_T < 2$ GeV/c in Pb+Pb collisions at $\sqrt{s_{NN}} = 2.76$ TeV in the AMPT+Hydro model (blue open circles) with $\eta/s = 0.12$ as compared to the ATLAS data [83] (red solid circles). The data points (starting at bottom left) correspond to fourteen 5% centrality intervals over the centrality range 0–70 %. The inset shows ε_2-ε_3 correlation as a function of centrality in the model calculations.
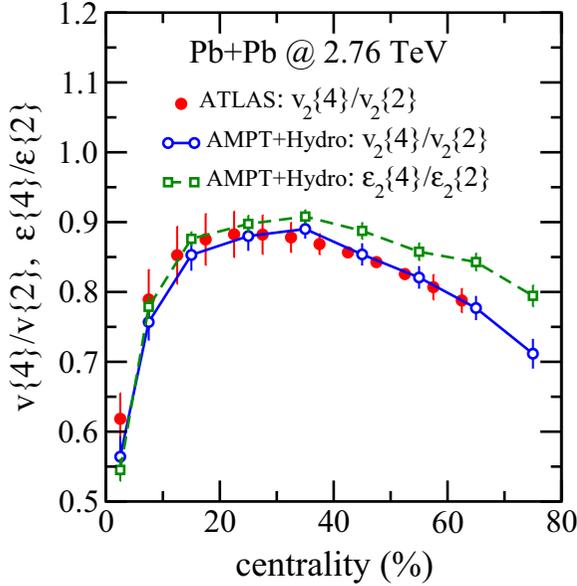
FIG. 10. The centrality dependence of the ratio $v_2\{4\}/v_2\{2\}$ for the elliptic flow obtained from two-and four-particle cumulant method in Pb+Pb collisions at $\sqrt{s_{NN}} = 2.76$ TeV in the AMPT+Hydro model (blue open circles) with $\eta/s = 0.12$ as compared to the ATLAS data [84] (red solid circles). Also shown is the ratio $\varepsilon_2\{4\}/\varepsilon_2\{2\}$ for the eccentricities in the model calculations (green open squares).

at centralities around ∼40–45 %, thereafter the harmonics v_2 and v_3 both decrease. Here, the conversion of initial spatial asymmetry to final momentum anisotropy is less efficient due to short lifetime of the plasma, especially for ε_3 that originates from small-scale structures (fluctuations).

Finally, we study event-by-event elliptic flow fluctuations. Cumulants [85] of the distribution of v_2 differ from one another if v_2 fluctuates event to event [86]. The relative fluctuations can be measured through the ratio of the first two cumulants, $v_2\{4\}/v_2\{2\}$. The fluctuations of v_2 originate to a large extent from the fluctuations of the initial eccentricity ε_2 [87]. If v_2 is proportional to ε_2, that is, if v_2/ε_2 is the same for all events in a centrality class [88], then $v_2\{4\}/v_2\{2\}$ coincides with $\varepsilon_2\{4\}/\varepsilon_2\{2\}$. Event-by-event hydrodynamics allows to directly test this relation by computing both quantities.

In Fig. 10, we compare the centrality dependence of the initial and final cumulant ratios, $\varepsilon_2\{4\}/\varepsilon_2\{2\}$ and $v_2\{4\}/v_2\{2\}$, in Pb+Pb collisions at $\sqrt{s_{NN}} = 2.76$ TeV in the AMPT+hydro model. The ratios coincide for central collisions, but $v_2\{4\}/v_2\{2\}$ becomes smaller than $\varepsilon_2\{4\}/\varepsilon_2\{2\}$ as the centrality percentile increases. This trend has already been observed in hydrodynamic calculations [89] and attributed to a nonlinear (cubic) response [90]. Our results are in excellent agreement with ATLAS data [84] over the entire centrality range. Note that they would not agree if v_2 was simply proportional to ε_2 in every event, as already observed with a different model of initial conditions [89]. This suggests that the success of hydrodynamics in describing elliptic flow fluctuations extends beyond a mere linear response to the initial eccentricity.

V. CONCLUSIONS

We have studied the effects of preequilibrium dynamics in heavy-ion collisions by modeling the early stages using a transport calculation with realistic cross sections, and coupling it to a (2+1)-dimensional viscous hydrodynamic calculation to describe the later evolution. Our model of the initial stage describes the microscopic dynamics of quarks and antiquarks as soon as they are produced, as modeled in AMPT. The initialization of the hydrodynamic calculation takes into account the fact that the transverse momenta of partons at a given point do not add up to zero and that they are not in local equilibrium: initial transverse flow and initial shear pressure are thus naturally taken into account. We have thus set up a comprehensive framework to perform calculations, which couples consistently initial stage dynamics and hydrodynamic evolution.

We have studied the effects of preequilibrium dynamics by switching off its components one by one. Initial transverse flow results in harder momentum spectra and larger anisotropic flow. This effect is more pronounced if the switching time from AMPT to hydrodynamics is delayed. The initial shear viscous pressure $\pi^{\mu\nu}$ has a much smaller effect: this is explained by our observation that various initializations of $\pi^{\mu\nu}$ relax to a common value at an early time ($\tau - \tau_{sw}) \simeq 1$ fm/c) and remain similar in magnitude thereafter. When the full preequilibrium dynamics is taken into account in initializing the hydrodynamic calculation, final results are insensitive to the choice of the switching time.

The model, with full initial dynamics ($v_T \neq 0 \neq \pi^{\mu\nu}$), describes identified particle spectra and differential anisotropic flow $v_n(p_T)(n = 2$–$6)$ at various centralities for Pb+Pb collisions at the LHC, with a constant shear viscosity to entropy density ratio of $\eta/s = 0.12$. We have also tested our formalism against quantities that had not yet been computed in the AMPT+hydro framework, in particular event-plane correlations and elliptic flow fluctuations, which probe the initial conditions and the hydrodynamic response in an independent way. Our calculations for these quantities are also in excellent agreement with LHC data. This overall agreement suggests that the AMPT model provides a reasonable description of the early stages of nucleus-nucleus collisions, and confirms the usual statement that the quark-gluon plasma produced at the LHC has a low shear viscosity over entropy ratio.

[1] J. Adams *et al.* (STAR Collaboration), Nucl. Phys. A **757**, 102 (2005).

[2] K. Adcox *et al.* (PHENIX Collaboration), Nucl. Phys. A **757**, 184 (2005).

[3] K. Aamodt *et al.* (ALICE Collaboration), Phys. Rev. Lett. **107**, 032301 (2011).

[4] G. Aad *et al.* (ATLAS Collaboration), Phys. Rev. C **86**, 014907 (2012).

[5] S. Chatrchyan *et al.* (CMS Collaboration), Phys. Rev. C **89**, 044906 (2014).

[6] W. Israel and J. M. Stewart, Ann. Phys. (NY) **118**, 341 (1979).

[7] A. Muronga, Phys. Rev. C **69**, 034903 (2004).

[8] P. Romatschke and U. Romatschke, Phys. Rev. Lett. **99**, 172301 (2007).

[9] H. Song and U. W. Heinz, Phys. Rev. C **77**, 064901 (2008).

[10] U. Heinz and R. Snellings, Ann. Rev. Nucl. Part. Sci. **63**, 123 (2013).

[11] P. K. Kovtun, D. T. Son, and A. O. Starinets, Phys. Rev. Lett. **94**, 111601 (2005).

[12] E. Retinskaya, M. Luzum, and J. Y. Ollitrault, Phys. Rev. C **89**, 014902 (2014).

[13] J. S. Moreland, J. E. Bernhard, and S. A. Bass, Phys. Rev. C **92**, 011901 (2015).

[14] J. Vredevoogd and S. Pratt, Phys. Rev. C **79**, 044915 (2009).

[15] J. Liu, C. Shen, and U. Heinz, Phys. Rev. C **91**, 064906 (2015); **92**, 049904(E) (2015).

[16] T. Epelbaum and F. Gelis, Phys. Rev. Lett. **111**, 232301 (2013).

[17] W. Florkowski and R. Ryblewski, Phys. Rev. C **83**, 034907 (2011).

[18] M. Martinez and M. Strickland, Nucl. Phys. A **848**, 183 (2010).

[19] W. van der Schee, P. Romatschke, and S. Pratt, Phys. Rev. Lett. **111**, 222302 (2013).

[20] L. Keegan, A. Kurkela, A. Mazeliauskas, and D. Teaney, J. High Energy Phys. 08 (2016) 171.

[21] A. Kurkela, A. Mazeliauskas, J.-F. Paquet, S. Schlichting, and D. Teaney, Nucl. Phys. A **967**, 289 (2017).

[22] H. Mäntysaari, B. Schenke, C. Shen, and P. Tribedy, Phys. Lett. B **772**, 681 (2017).

[23] C. Gale, S. Jeon, B. Schenke, P. Tribedy, and R. Venugopalan, Phys. Rev. Lett. **110**, 012302 (2013).

[24] R. D. Weller and P. Romatschke, Phys. Lett. B **774**, 351 (2017).

[25] Z. W. Lin, C. M. Ko, B. A. Li, B. Zhang, and S. Pal, Phys. Rev. C **72**, 064901 (2005).

[26] L. Pang, Q. Wang, and X. N. Wang, Phys. Rev. C **86**, 024911 (2012).

[27] R. S. Bhalerao, A. Jaiswal, and S. Pal, Phys. Rev. C **92**, 014903 (2015).

[28] W. Zhao, H.-J. Xu, and H. Song, Eur. Phys. J. C **77**, 645 (2017).

[29] C. Shen, Z. Qiu, H. Song, J. Bernhard, S. Bass, and U. Heinz, Comput. Phys. Commun. **199**, 61 (2016).

[30] J. Adam *et al.* (ALICE Collaboration), Phys. Rev. Lett. **119**, 102301 (2017).

[31] J. Xu and C. M. Ko, Phys. Rev. C **84**, 044907 (2011).

[32] S. Pal and M. Bleicher, J. Phys. Conf. Ser. **420**, 012027 (2013).

[33] L. Adamczyk *et al.* (STAR Collaboration), Phys. Rev. C **88**, 014902 (2013).

[34] R. S. Bhalerao, J. Y. Ollitrault, and S. Pal, Phys. Rev. C **88**, 024909 (2013).

[35] G. Aad *et al.* (Atlas Collaboration), Phys. Rev. C **90**, 024905 (2014).

[36] S. Acharya *et al.* (ALICE Collaboration), Phys. Rev. C **97**, 024906 (2018).

[37] W. T. Deng, X. N. Wang, and R. Xu, Phys. Rev. C **83**, 014915 (2011).

[38] S. Pal and M. Bleicher, Phys. Lett. B **709**, 82 (2012).

[39] X. N. Wang and M. Gyulassy, Phys. Rev. D **44**, 3501 (1991).

[40] B. Zhang, Comput. Phys. Commun. **109**, 193 (1998).

[41] J. D. Bjorken, Phys. Rev. D **27**, 140 (1983).

[42] B. Alver *et al.* (PHOBOS Collaboration), Phys. Rev. C **81**, 034915 (2010).

[43] S. Chatrchyan *et al.* (CMS Collaboration), Eur. Phys. J. C **72**, 2012 (2012).

[44] P. Bozek, W. Broniowski, and J. Moreira, Phys. Rev. C **83**, 034911 (2011).

[45] H. Petersen, V. Bhattacharya, S. A. Bass, and C. Greiner, Phys. Rev. C **84**, 054908 (2011).

[46] K. Xiao, F. Liu, and F. Wang, Phys. Rev. C **87**, 011901(R) (2013).

[47] J. Jia and P. Huo, Phys. Rev. C **90**, 034915 (2014).

[48] L.-G. Pang, G. Y. Qin, V. Roy, X. N. Wang, and G. L. Ma, Phys. Rev. C **91**, 044904 (2015).

[49] L.-G. Pang, H. Petersen, G.-Y. Qin, V. Roy, and X.-N. Wang, Eur. Phys. J. A **52**, 97 (2016).

[50] V. Khachatryan *et al.* (CMS Collaboration), Phys. Rev. C **92**, 034911 (2015).

[51] M. Aaboud *et al.* (ATLAS Collaboration), Eur. Phys. J. C **78**, 142 (2018).

[52] P. Bozek and W. Broniowski, arXiv:1711.03325.

[53] J. Steinheimer, M. Bleicher, H. Petersen, S. Schramm, H. Stocker, and D. Zschiesche, Phys. Rev. C **77**, 034901 (2008).

[54] P. Romatschke, Int. J. Mod. Phys. E **19**, 1 (2010).

[55] P. Huovinen and P. Petreczky, Nucl. Phys. A **837**, 26 (2010).

[56] M. Luzum and P. Romatschke, Phys. Rev. C **78**, 034915 (2008); **79**, 039903(E) (2009).

[57] F. Cooper and G. Frye, Phys. Rev. D **10**, 186 (1974).

[58] D. Teaney, Phys. Rev. C **68**, 034913 (2003).

[59] H. Niemi, K. J. Eskola, and R. Paatelainen, Phys. Rev. C **93**, 024907 (2016).

[60] K. Aamodt *et al.* (ALICE Collaboration), Phys. Rev. Lett. **105**, 252302 (2010).

[61] W. Broniowski and W. Florkowski, Phys. Rev. C **65**, 024905 (2002).

[62] S. A. Voloshin and A. M. Poskanzer, Phys. Lett. B **474**, 27 (2000).

[63] D. Teaney and L. Yan, Phys. Rev. C **83**, 064904 (2011).

[64] P. F. Kolb, J. Sollfrank, and U. W. Heinz, Phys. Rev. C **62**, 054909 (2000).

[65] J. Y. Ollitrault, Phys. Rev. D **46**, 229 (1992).

[66] H. Sorge, Phys. Rev. Lett. **78**, 2309 (1997).

[67] U. Heinz, Z. Qiu, and C. Shen, Phys. Rev. C **87**, 034913 (2013).

[68] B. Abelev *et al.* (ALICE Collaboration), Phys. Rev. C **88**, 044910 (2013).

[69] J. Noronha-Hostler, M. Luzum, and J. Y. Ollitrault, Phys. Rev. C **93**, 034912 (2016).

[70] J. Y. Ollitrault, A. M. Poskanzer, and S. A. Voloshin, Phys. Rev. C **80**, 014904 (2009).

[71] L. X. Han, G. L. Ma, Y. G. Ma, X. Z. Cai, J. H. Chen, S. Zhang, and C. Zhong, Phys. Rev. C **84**, 064907 (2011).

[72] A. Bzdak and G. L. Ma, Phys. Rev. Lett. **113**, 252301 (2014).

[73] V. Y. Naboka, I. A. Karpenko, and Y. M. Sinyukov, Phys. Rev. C **93**, 024902 (2016).

[74] J. Adam *et al.* (ALICE Collaboration), Phys. Rev. Lett. **116**, 132302 (2016).

[75] S. McDonald, C. Shen, F. Fillion-Gourdeau, S. Jeon, and C. Gale, Phys. Rev. C **95**, 064913 (2017).

[76] J. Jia (ATLAS Collaboration), Nucl. Phys. A **910-911**, 276 (2013).

[77] D. Teaney and L. Yan, Phys. Rev. C **90**, 024902 (2014).

[78] S. Acharya *et al.* (ALICE Collaboration), Phys. Lett. B **773**, 68 (2017).

[79] M. Luzum and J. Y. Ollitrault, Phys. Rev. C **87**, 044907 (2013).

[80] L. Yan and J. Y. Ollitrault, Phys. Lett. B **744**, 82 (2015).

[81] L. Yan, S. Pal, and J. Y. Ollitrault, Nucl. Phys. A **956**, 340 (2016).

[82] Z. Qiu and U. Heinz, Phys. Lett. B **717**, 261 (2012).

[83] G. Aad *et al.* (ATLAS Collaboration), Phys. Rev. C **92**, 034903 (2015).

[84] G. Aad *et al.* (ATLAS Collaboration), Eur. Phys. J. C **74**, 3157 (2014).

[85] N. Borghini, P. M. Dinh, and J. Y. Ollitrault, Phys. Rev. C **64**, 054901 (2001).

[86] M. Miller and R. Snellings, arXiv:nucl-ex/0312008.

[87] B. Alver *et al.* (PHOBOS Collaboration), Phys. Rev. Lett. **98**, 242302 (2007).

[88] H. Niemi, G. S. Denicol, H. Holopainen, and P. Huovinen, Phys. Rev. C **87**, 054901 (2013).

[89] G. Giacalone, J. Noronha-Hostler, and J. Y. Ollitrault, Phys. Rev. C **95**, 054910 (2017).

[90] J. Noronha-Hostler, L. Yan, F. G. Gardim, and J. Y. Ollitrault, Phys. Rev. C **93**, 014909 (2016).